Heliyon 10 (2024) e31353

Contents lists available at ScienceDirect

Heliyon

journal homepage: www.cell.com/heliyon

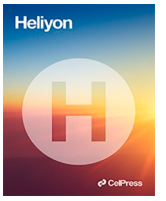

Research article

The coupled WO_3-AgBr nanocatalyst, part II: Synthesis, characterization, and the boosted photocatalytic activity towards metronidazole in an aqueous solution

Elaheh Shabanian-Broujeni [a], Alireza Nezamzadeh-Ejhieh [a,b,*]

[a] Department of Chemistry, Shahreza Branch, Islamic Azad University, 311-86145, Shahreza, Isfahan, Iran
[b] Razi Chemistry Research Center (RCRC), Shahreza Branch, Islamic Azad University, Isfahan, Iran

ARTICLE INFO

Keywords:
AgBr-WO_3 coupled catalyst
Band gap energy
Potential position of valence and conduction bands
Heterogenous photodegradation

ABSTRACT

The AgBr and WO_3 nanoparticles (NPs) were synthesized and coupled, and the coupled AgBr-WO_3 binary catalyst, as well as the individual AgBr and WO_3 NPs, were then characterized by XRD, FTIR, DRS, and SEM-EDX. XRD results showed the formation of orthorhombic WO_3 cubic AgBr crystals. The crystallite sizes of 45, 28, and 45 nm were estimated by the Scherrer formula for the as-prepared AgBr, WO_3, and AgBr-WO_3 catalysts, respectively. The DRS study estimated band gap energies using both absorption edge wavelengths and the Kubelka-Munk model. The band gap energies of 2.72, 3.06, and 2.92 eV were obtained for the direct electronic transitions of AgBr, WO_3, and AgBr-WO_3. The E_{CB} (potential position) of AgBr and WO_3 were estimated to be 0.01 and 0.52 V, while their E_{VB} values were 2.60 and 3.55 V, respectively. Typical FTIR absorption bands of W–OH, the W–O–W, and AgBr bonds have appeared at 1637 cm^{-1}, 823 (and 766) cm^{-1}, and 1384 $cm^{-1,}$ respectively. The pHpzc of 4 was estimated for the individual and coupled catalysts. In studying the photocatalytic activity of the catalysts in the photodegradation of metronidazole (MNZ) a boosted activity was achieved for the coupled system. This increased activity depends on the maximum AgBr:WO_3 mole ratio in a 1:3 mol ratio. Grinding time applied to prepare the coupled catalyst has also varied the photocatalytic activity.

1. Introduction

Exploring environmental pollution has resulted in novel strategies for removing various pollutants from aquatic environments in recent years [1–6]. The pharmaceutical industries, hospitals, and domestic sites discharge the effluents containing various pharmaceutics, such as antibiotics, into surface and ground waters with low biodegradability. This needs to introduce novel techniques/catalysts to remove these pollutants from wastewater [7–14].

Generally, the accumulated MTZ in animals, fish farm water, and effluents resulted from meat industries, and due to its non-biodegradability and high water solubility features, its accumulation in the aquatic environment is high. Remained MNZ in surface waters and wastewater ranges from 1 to 10 ng/L. In contrast, it has proven its low concentrations have toxic effects on aquatic organisms like algae and daphnids. The MNZ Genotoxic effects of MTZ have been proven on *Oreochromis niloticus* and for other organs of

* Corresponding author: Department of Chemistry, Shahreza Branch, Islamic Azad University, 311-86145, Shahreza, Isfahan, Iran.
E-mail addresses: elahehshabanian97@gmail.com (E. Shabanian-Broujeni), arnezamzadeh@iaush.ac.ir, arnezam1346@gmail.com, Alireza_nezamzadeh@yahoo.com (A. Nezamzadeh-Ejhieh).

https://doi.org/10.1016/j.heliyon.2024.e31353
Received 26 January 2024; Received in revised form 8 May 2024; Accepted 15 May 2024
Available online 16 May 2024

fish. Some adverse effects of MNZ on beneficial bacteria in biological filtrate have been confirmed. Anaerobic bacteria convert nitrate to nitrous gas as the last step of the nitrogen cycle in biological filtration in aquaria. This step can be prevented in the presence of MNZ, resulting in nitrate accumulation, causing infection, some physiological stresses, inducing the immune system and damaging tissue in aquatic organisms, incomplete blood O_2 transport, and renal insufficiency. Thus, before this process, MNZ should be removed from the solution. An increased corticotrophin-releasing factor, cortisol, and ACTH secretions would result in acute stress conditions. In contrast, the activation of the cell population of the central immune system increases the release of cytokines, chemokines, growth factors, arachidonic acid, and reactive oxygen species (ROSs) like nitrite oxide. Thus, a critical issue is its elimination from the water system because of its high toxicity (toxic effects on aquatic and terrestrial organisms), potential mutagenicity, and carcinogenetic (as an animal carcinogen) features [15–17].

The semiconducting-based photocatalytic degradation has been well-known effective removal technique for various organic pollutants based on inducing the photoexcited electrons in the conduction band (CB) and the leaved holes in the valence band (VB) under the UV or visible lights' illumination of the semiconductor used [18–27]. The e^-/h^+ pairs induced can directly reduce or oxidize molecules of pollutants and begin their degradation reaction. Indirectly, photoinduced electrons produce the dissolved oxygen to form superoxide radicals. The holes can oxidize water molecules to form hydroxyl radicals as powerful agents for degrading organic molecules as pollutants [28–34].

To have an efficient heterogeneous photodegradation, a sufficient charge carriers (e^-/h^+) separation would be achieved because the recombination of the photogenerated e^-/h^+ pairs can significantly decrease the overall photodegradation efficiency [35–41]. Various strategies have been suggested to decrease e/h recombination like metal/nonmetal doping, supported semiconductors, coupled semiconductors systems, and nano-dimension catalysts, etc. [42–59].

An important effective photosensitive material that is extensively used in photography and photocatalysis technologies is silver halides AgX (X = Cl, Br, I). The generation of high amounts of e−/h + pairs under visible illumination of AgBr converts it into a potential visible light photocatalyst [60]. However, its practical applications have been limited due to the photodecomposition of pure AgBr. A common way to diminish this drawback is by supporting AgX species on some substrates, like SiO_2 [61], zeolites [62], Fe_3O_4 [62], Bi_2WO_6 [63,64], etc. These composites display high e^-/h^+ separation and, thus, high photocatalytic activity with relatively enhanced optical stability [63]. This boosted effect can also be related to forming a heterojunction structure between AgX and substrate [65]. The band gap energy of WO_3 is around 3.03 eV [66] and AgBr around 2.59 eV [67]. WO_3 has a lower (more positive) conduction band (0.52 eV) than that of AgBr (0.01), while a lower (more positive) VB potential position (3.55 eV) than that of AgBr (2.60 eV) [68]. These matched potential positions make it suitable to construct AgBr/WO_3 composite/heterojunction structure with good e^-/h^+ pairs' separation ability [69].

Detailed photodegradation results and mechanisms are illustrated in this work's first part after briefly characterizing this binary catalyst [70]. In the present work, the mechanically AgBr/WO_3 coupled catalyst, a visible-light-driven photocatalyst, was prepared in situ, and its photocatalytic activity was evaluated toward metronidazole (MNZ) in an aqueous phase.

2. Experimental

2.1. Chemicals

The main chemicals sodium tungstate (Na_2WO_4. $2H_2O$), $AgNO_3$, NaBr, HCl, etc., purchased from Sigma/Aldrich company, all have an analytical grade purity. The metronidazole table (Iran Daru Co., IRAN) was prepared at local drugstores. Aqueous solutions/suspensions were obtained in distilled water, and their pH was adjusted by diluting NaOH or HCl solution.

To prepare the MNZ solution, the average weight of each 250 mg metronidazole pharmaceutical tablet (Iran Daru Co., Iran) was about 0.3155 g. Four tablets were ground in an agate mortar to have a homogeneous powder, and 0.0315 g of the powder was added to a 100 mL beaker and dissolved in 50 mL water under a string for 15 min. Then, it was filtered into a 250 mL volumetric flask and reached the mark by water. This solution was 100 mg/L concerning MNZ and was used to prepare diluter solutions via the serial dilution procedure.

2.2. Synthesis of nanoparticles

In AgBr NPs synthesis, solution A was 50 mL 0.1 M $AgNO_3$, while solution B was 20 mL 0.25 M NaBr. After mixing, it was kept at 60 °C for 1 h under stirring. A golden yellow precipitate was obtained that was separated by centrifugation. It was thoroughly washed with water and ethanol and vacuum-dried [71].

In a typical procedure for synthesizing WO_3 NPs, 20 mL 8 M HCl solution was added to a 20 mL sodium tungstate solution containing 3 g of $Na_2WO_4{\cdot}2H_2O$. Subsequently, a yellowy dispersion was formed that was transferred into a 50 mL Teflon-lined stainless-steel autoclave. The autoclave was placed at 100 °C for 24 h. Finally, the yellowish precipitate was separated by centrifuge, thoroughly water-washed, and then ethanol. After drying at 80 °C, it was calcined at 400 °C for 4 h to obtain WO_3 NPs [72].

To prepare the AgBr – WO_3 binary catalyst, depending on the AgBr:WO_3 mole ratio requested, an adequate weight of each component was added to an agate mortar and thoroughly hand-mixed for 15 min to obtain a homogeneous powder [73].

2.3. Determination of pHpzc

Series suspensions containing 0.015 g of each AgBr or WO_3 NPs or AgBr-WO_3 coupled system in 10 mL 0.01 M NaCl (as ionic

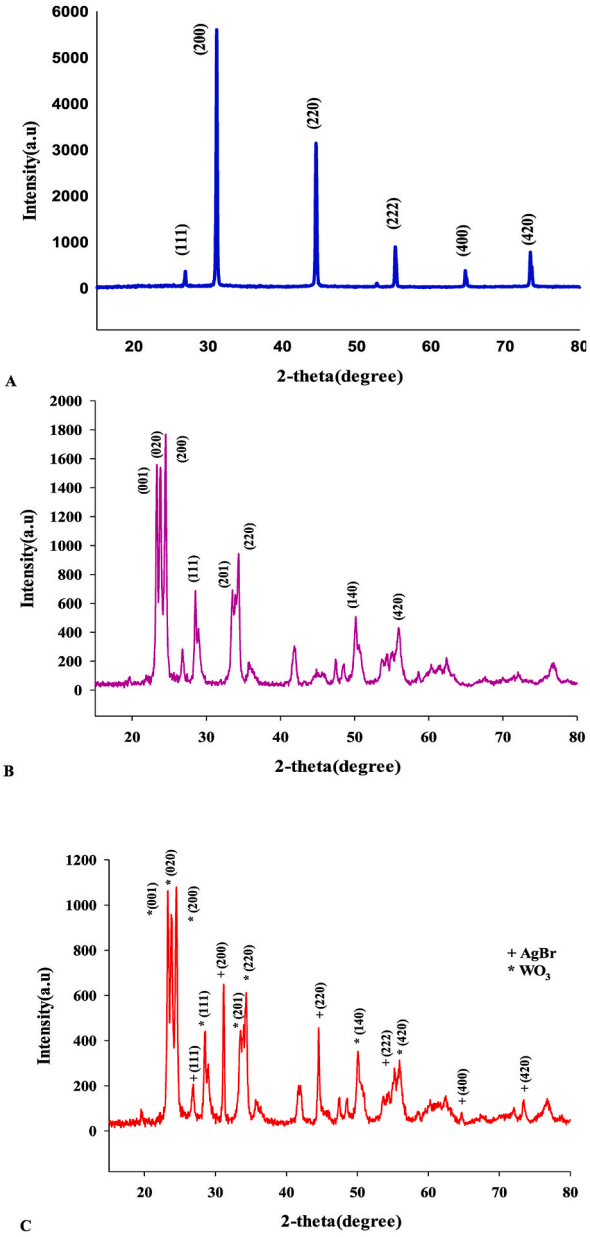

Fig. 1. The XRD pattern of the **(A)** single AgBr NPs, **(B)** single WO_3 NPs, and **(C)** the binary AgBr – WO_3 catalyst with a AgBr:WO_3 mole ratio of 1:3 [70].

strength adjuster) were prepared. After adjusting the pH range from 2 to 12 by diluting HCl or NaOH solution (pH initial: pH_I), and shaking for about 24 h, the final pH (pH_F) was recorded. Two typical plots were constructed (see results and discussion section) to determine the pHpzc. In the first one, pH_F was plotted against pH_I. The bisector of this plot was achieved by plotting pH_I versus pH_I. The crossing point of each curve with bisector gives the pHpzc for each catalyst. In the second plot, ΔpH (ΔpH is the difference between the pH_F –pH_I regarding the sign obtained) was plotted versus pH_I. The point in which $\Delta pH = 0$ is the pHpzc of the related catalyst.

2.4. Instruments and characterization

Following instruments were used here: X-ray diffractometer (X'PertPro, Ni-filtered Cu-Ka radiation at 1.5406 Å, V: 40 kV, i: 30 mA; Netherland), FTIR (PerkinElmer Spectrum 65 and KBr pellet), UV–Vis diffuse reflectance spectrophotometer (JASCO V 670, against $BaSO_4$ reference, Japan), a scanning electron microscope (TESCAN, model MIRA3, Co Czech Republic), a double beam UV–Vis

PerkinElmer spectrophotometer, a pH meter/p-ion meter (Jenway model 3505), and a centrifuge instrument (Sigma, rpm: 13,000, g: 15,493).

2.5. Photodegradation experiments

A homemade reaction box was assembled to run the photocatalytic degradation experiments. In a typical photodegradation run, 10 mL 5 ppm MNZ aqueous solution was prepared, which was 0.5 g/L for each single or coupled catalyst. Then, it was subjected to illumination against three 40 W W-lamps. The distance with the reaction of the 25 mL glass reaction beaker as a cell was 10 cm above the sample cell. Under continuous magnetic stirring, a homogeneous suspension was achieved to produce a constant mass transfer. At regular times, for example, for 30 min in the initial removal tests, sampling was done, and the suspension was centrifuged (at >13,000 rpm) to obtain a clean solution that was suitable to record the absorbance at absorption band maximum of MNZ (320 nm). The absorbance of the photodegraded MNZ solution at time t was A, which was compared against that of the blank MNZ solution without any catalyst and illumination (A_o) to calculate the (A/A_o) value or the degradation extent of MNZ molecules by the following formula (Eq. 1). Based on the Beer-Lambert law, this is based on the straight proportionality of absorbance and analyte concentration. Before the illumination, dark stirring for 10 min was made to achieve a surface adsorption/desorption equilibrated state.

$$\text{Degradation efficiency (\%)} = [(C_o\text{-}C)/C_o)] \times 100 = [(A_o\text{-}A)/A_o)] \times 100 \quad (1)$$

3. Results and discussion

3.1. Characterization of the samples

3.1.1. XRD patterns

As-synthesized WO_3 and AgBr NPs and the as-prepared coupled sample were subjected to diffraction analysis to estimate phase purity. The diffraction patterns obtained via the powder x-ray diffraction analysis are shown and compared in Fig. 1A–C. In the pattern of AgBr alone (Fig. 1A), a cubic crystallite phase was detected because the diffraction peaks at 26.8°, 31.1°, 44.6°, 55.4°, 64.7°, and 73.5° agreed well with that of standard pattern with the JCPDS No. 06-0438 [74]. The diffraction peaks mentioned relate to the diffraction planes of (111), (200), (220), (222), (400), and (420), respectively, which are assigned in the pattern [70].

When the XRD pattern of WO_3 NPs (Fig. 1B) was compared to the standard patterns, the diffraction peaks at 23.1°, 23.7°, 24.1°, 28.8°, 33.6°, 34°, 50° and 55.4° overlapped with those reported for the orthorhombic structure of WO_3 with the standard pattern of JCPDS No. 20-1324 [75]. The peaks mentioned above, which belong to the crystal planes of (001), (020), (200), (111), (201), (220), (140), and (420), were respectively assigned to their corresponding *hkl* planes [70].

As shown in the pattern for the binary coupled AgBr/WO_3 catalyst (Fig. 1C), all of the peaks mentioned above for the individual AgBr and WO_3 NPs have appeared. This infers that the AgBr/WO_3 binary system is prepared by a mechanical force induced during the grinding of the mixture [76]. The overall peak intensity decreased because of higher amounts of WO3 NPs in the catalyst (AgBr:WO_3 mole ratio of 1:3).

Both size and stain broadenings were evaluated by subjecting the XRD results to the Scherrer (Eq. (2)) and the Williamson-Hall (W-H) (Eq. (3)) equations. Equation (2), the common Scherer formula, is useable to study the effect of size broadening in a diffraction peak. General use of the Scherrer formula has been restricted for estimating crystallite sizes less than 100 nm. In this formula, the inverse relationship of d (crystallite size in nm) with the diffraction width peak, β, confirms the appearance of broader peaks for nanomaterials than the bulk materials [77].

$$d = \frac{k.\lambda}{\beta.cos\theta} \quad (2)$$

All data used for this calculation, including the half of diffraction angle θ and β values, are summarized in SDT1 (see supplementary data). Although the Scherer constant k gets different values between 0.8 and 1.1 depending on the shape of the crystals, its typical value is 0.9, which is used in our calculations. The X-ray wavelength (λ) used is the Cu-Kα line at 0.15406 nm [78,79]. The average sizes for crystals of AgBr, WO_3, and AgBr–WO_3 were estimated around 45, 28, and 28 nm, respectively.

Commonly, the d-spacing for its *hkl* planes can occur by the probable sample deformation, which results in slight shifts in the peak positions and the lattice strain. This strain is induced by the dislocation-like defects, while the size broadening results from the shrinkage of coherent scattering volume [80,81].

It seems that the induced mechanical force applied in the preparation of binary AgBr–WO_3 catalyst induces some strain on the crystals, resulting in d-spacing change. As the Braggs' law ($n\lambda = 2d\sin\theta$) confirms, due to this d-fluctuation, the brag angle θ would be changed. In such a case, it is better to use the Williamson-Hall (W-H) model (formula 3) to estimate the crystallite size [82,83].

$$\beta.\cos\theta = (k\lambda/d) + (\eta/\sin\theta) \quad (3)$$

W-H model includes the Scherer term ($k\lambda/d$) and the internal strain or Stokes and Wilson expression ($\eta/\sin\theta$). Commonly, the crystallite size, induced strain, instrumental parameters, and crystal defects have been counted as the influencing factors on the diffraction peak broadening. The W-H model gives the Scherer model in a particular strain factor η = zero case [84–86].

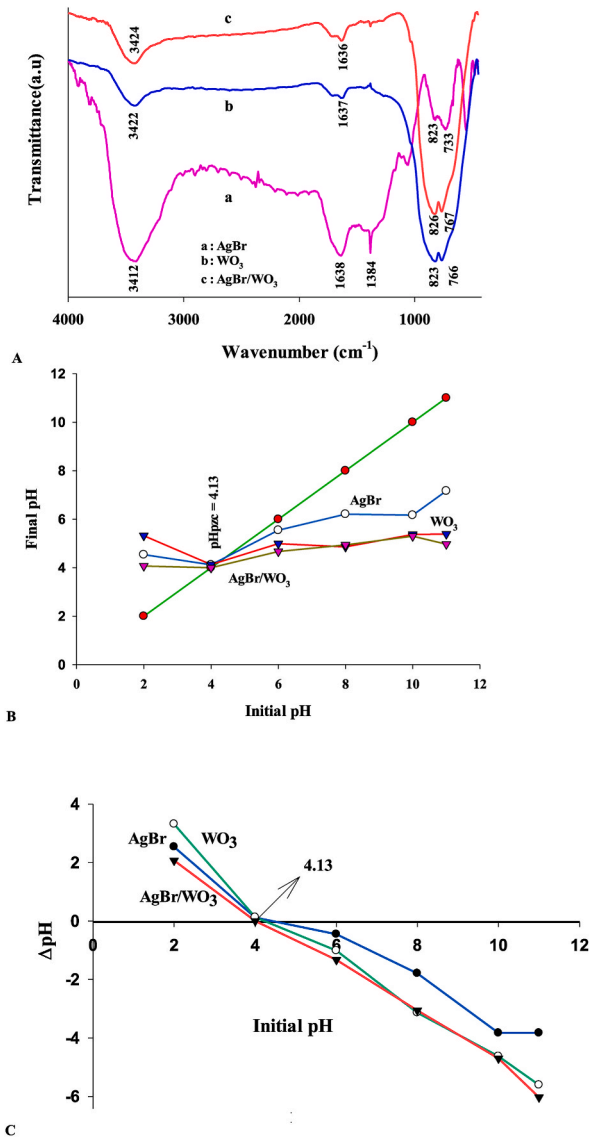

Fig. 2. FTIR spectra of the individual and the composite samples **(A)**; Typical plots for determining the samples' pHpzc **(B-C)** [70].

SDT2 shows data used/calculated for plotting the W–H curves, a plot of $\beta\cos(\theta)$ versus $\sin(\theta)$. The plots are shown in SDF1 [85,87,88]. The intercept of the curves was used to estimate the crystallite size for AgBr, WO_3, and AgBr–WO_3 samples that obtained about 5, 6, and 6 nm, respectively. The difference between values obtained by the Scherrer and W-H model can be considered as the evidence for induced strain due to mechanical force.

3.1.2. FTIR spectra

Fig. 2A compares FTIR (Fourier transform infrared) spectra for the as-prepared individual and coupled catalysts. In the WO_3 spectrum, the main vibrational futures relate to W–OH and the W–O–W bonds. The first bond appeared as an absorption band for the bending mode at 1637 cm^{-1}. This bending vibrational mode has appeared at 1630 cm^{-1} in the literature. The strong absorption bands at 823 and 766 cm^{-1} can relate to the W–O–W vibrational stretching modes [89]. The appearance of these characteristics proves the successful synthesis of WO_3. The typical stretching vibration mode for AgBr appears at 1384 cm^{-1} in its spectrum [90]. Other stretching or bending absorption bands are due to the adsorbed water (stretching about 3500 and bending around 1637 cm^{-1}), or C-C and C-H bonds [91,92], etc., of or4aganic materials used in the synthesis procedures, remained as surface adsorbed species. All peaks mentioned above with slight shifts or broadening have appeared in the spectrum of the coupled sample. FTIR spectra are briefly described in the first section of the work [70].

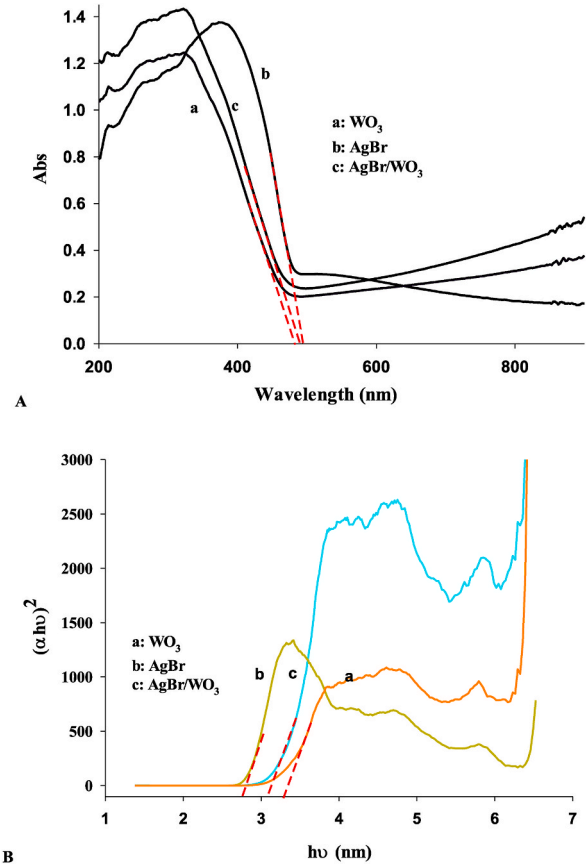

Fig. 3. Typical absorption spectra **(A)** and Tauc plots (for n = 2) **(B)** obtained in DRS study of the samples.

3.1.3. Point of zero charge (pH_{pzc})

A significant factor called the point of zero charge (pH_{pzc}) has been described to evaluate the absorption capacity of a typical absorbent/catalyst and its surface binding sites. Its usual utilization is to describe the kinetic futures of the surface. A favorable pH for the effective absorption of positive species/ions is $pH > pH_{pzc}$, while for absorbing positive species/ions, $pH < pH_{pzc}$ is favorable. This is because the accumulated net charges on the surface of the adsorbent/catalyst are different at pHs below and beyond the pHpzc value. Below it, the surface of the solid adsorbent/catalyst accumulated by the adsorbed protons due to its native negative of basic future. This results in an increase in the pH of the aqueous phase around the solid species. Above the pHpzc, negative charges accumulate due to the adsorbed hydroxyl radicals from the adjacent aqueous solution, which results in a net negative charge on the surface [93].

Typical plots for estimating the pHpzc value for the catalysts are shown in Fig. 2B and C. As shown, all catalysts investigated here have a pHpzc around 4.1.

3.1.4. DRS study

A common approach for estimating the band gap energy (Eg) for the various electronic transitions in a semiconducting material is recoding the DRS (diffuse reflectance spectroscopy) spectra. The macroscopic optical characteristics of materials can be extracted from DRS spectra, in general, including the overall samples' reflectance and absolute absorbance, as well as their dispersive features. The absorption characteristics obtained evaluate the sample's macroscopic optical properties and the extent of loss in samples' internally emitted light. On the other hand, the change in the absorption characteristics is because of the dependence of the diffused reflected (re-emitted) intensity on the samples' optical futures, particle size distribution, and filling factor [94].

The absorption spectra of the AgBr and WO_3 NPs and the AgBr/WO_3 coupled catalyst are presented in Fig. 3A. The downward slopes of the plots were extrapolated towards the photon energy wavelength (the x-axis). The cross point is called the absorption edge wavelength (λ_{AE}), which is substituted into the Eg (eV) = 1240/λ_{AE} (nm) formula to obtain the Eg value [95,96]. The results obtained are summarized in Table 1.

A common, more precise approach for determining Eg for a semiconducting material is using the absolute reflectance data of the solid powder sample obtained from DRS study, which should be transformed by a model well-known the Kubelka-Munk (K-M) model. The transformed data were then used to estimate Eg graphically for various electronic transitions of the semiconductor investigated by the following Tauc formula (Eq. 4). In this formula, h and υ are Planck's constant (J s), and the light frequency (s^{-1}), β is an absorption constant. At the same time, α is the absorption coefficient that can be obtained based on Beer–Lambert's law by the sample thickness

Table 1
Band gap and potential positions for CB and VB of the semiconductors used.

Approximated band gap energies of the used catalysts by using the absorption edge method and Kubelka-Munk equation and Tauc plots

Catalysts	Tauc plots (eV)				Absorption edge	
	1/2	2	3/2	3	λ (nm)	Eg (eV)
AgBr	2.46	2.72	2.77	2.84	495	2.51
WO_3	2.69	3.06	3.36	3.36	481	2.58
AgBr-WO_3	2.54	2.92	3.19	3.28	490	2.53

E_a and E_i values of the constituent elements of the used semiconductors

Element	E_a (eV)	E_i (eV)	½(E_a + E_i) (eV)
Ag	1.304	7.576	4.44
Br	3.365	11.831	7.590
W	0.816	7.864	4.34
O	1.461	13.618	7.539

Eg, V_B and C_B values of the used semiconductors, X data are in Mulliken's electronegativity scale

Catalyst	χ (eV)	Eg (eV)	E_{VB} (eV)	E_{CB} (eV)
AgBr	5.81	2.72	+2.67	−0.05
WO_3	6.54	3.06	+3.57	+0.51

Various models to write Tauc model

Formula	n-value for:				
	IF	IA	DF	DA	[Ref]
$F(R)\ h\upsilon = A\ (h\upsilon - Eg)^n$	3	2	3/2	1/2	[98]
$(F(R)\ h\upsilon)^n = A\ (h\upsilon - Eg)$	1/3	1/2	2/3	2	[99]
$(\alpha h\upsilon)^{1/n} = A\ (h\upsilon - Eg)$	3	2	3/2	1/3	[100–102]
$(\alpha h\upsilon) = A\ (h\upsilon - Eg)^{1/n}$	1/3	1/2	2/3	2	[103,104]
$(\alpha h\upsilon) = A\ (h\upsilon - Eg)^{n/2}$	6	4	3	1	[105]
$(\alpha h\upsilon)^{2/n} = A\ (h\upsilon - Eg)$	6	4	3	1	[105]

IF: Indirect forbidden, **IA**: Indirect allowed, **DF**: Direct forbidden, **DA**: Direct allowed.

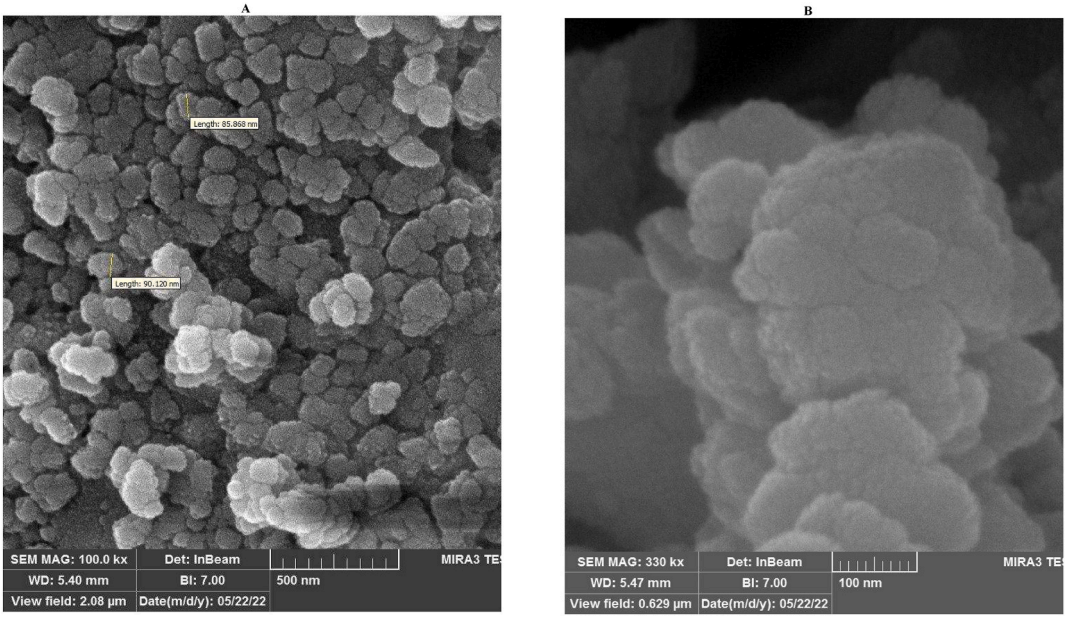

Fig. 4. SEM images **(A–B)**, particles size distribution **(C)**, EDX spectrum **(D)**, and x-ray map image **(E)** for the binary AgBr – WO_3 catalyst [70].

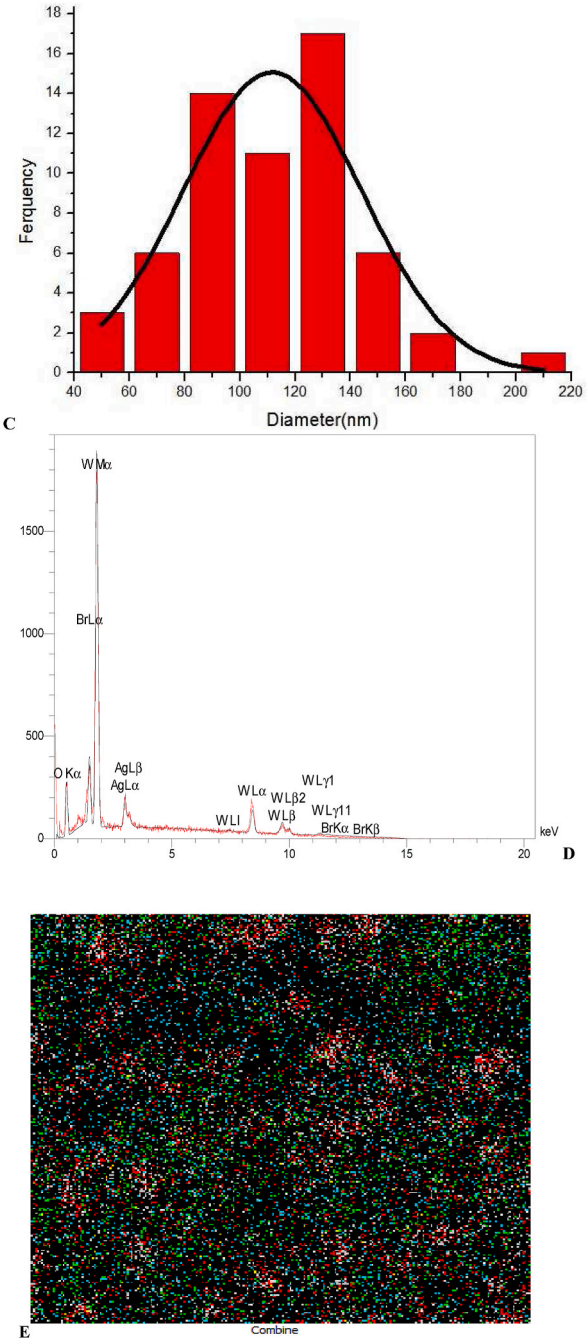

Fig. 4. (*continued*).

d and the sample absorbance A as α = ([2.303 × A]/d).

Various formats can formulate the Tauc model, summarized in Table 1, which are the same principle but various component terms. For example, for the following formula, depending on the electronic transition type, n gets different values of 1/2 (allowed direct: AD), 2 (allowed indirect: AI), 3/2 (forbidden direct: FD), and 3 (forbidden direct: FI) for the mentioned transitions [97].

$$(\alpha h\nu) = \beta\left(h\nu - E_g\right)^n \tag{4}$$

The obtained reflectance spectrum is presented in SDF1-A, and the Tauc plots in Fig. 2B and SDF2 B-D are typical plots of $(\alpha h\upsilon)^n$ vs hυ. These plots' rising slope was extrapolated towards the x-axis, the photon energy. This crossing point gives the $(\alpha h\upsilon)^n = 0$, in which hν = Eg. The obtained Eg values are summarized in Table 1.

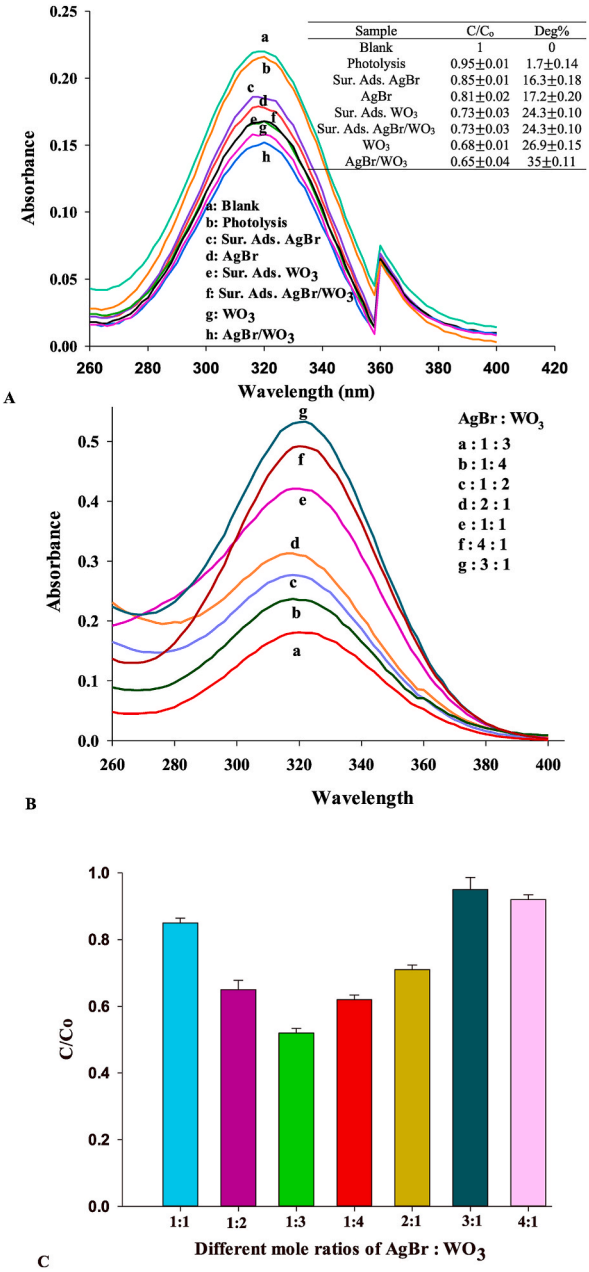

Fig. 5. Change in the UV–Vis absorbance of MNZ solutions during the various removal processes mentioned **(A)** [70]; The effect of the change in the change in AgBr:WO_3 mole ratio in the coupled system on the MNZ photodegradation: UV-Vis spectra of the photodegraded MNZ solutions **(B)** and the obtained C/Co values **(C).** All results were averaged based on triplicate measurements (Catalyst dose: 0.3 g/L, C_{MNZ}: 5 ppm, Illumination time: 45 min) [70].

Equation (5) was used to estimate the valence band edge position (E_{VB}) of AgBr and WO_3 using the Eg values obtained for the direct allow electronic transition, and the free electron energy (E_e: 4.5 eV vs NHE), and the electronegativity of the semiconductors (χ). To estimate χ, the geometric mean of the electronegativity of the semiconductors' constituent atoms was used. The arithmetic mean of the first atomic electron affinity (Ea) and the first ionization energy (Ei) was used to estimate the atoms' electronegativity. In general, this formula is suitable for calculating the E_{VB} of a semiconductor at the point of zero charge.

$$E_{VB} = \chi - E_e + 0.5E_g \quad (5)$$

The χ values for AgBr and WO_3 are ca. 5.81 and 6.54 eV, and the E_{VB} of AgBr and WO_3 were calculated to be 2.60 and 3.55 eV, respectively. Thus, the E_{CB} of AgBr and WO_3 were estimated to be 0.01 and 0.52 eV, respectively [68]. Then, E_{CB} was determined by

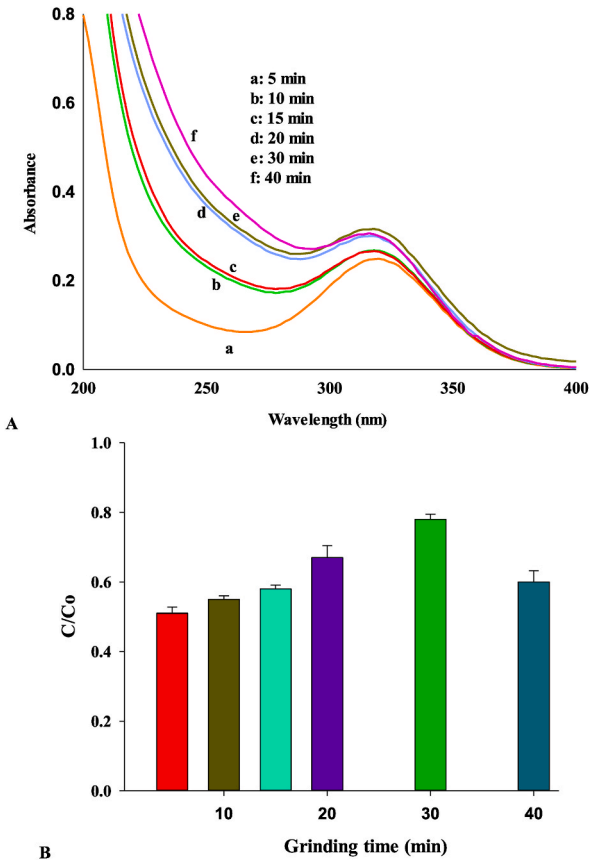

Fig. 6. The effect of the grinding time in the mechanical preparation of AgBr:WO_3 catalyst in the MNZ photodegradation: UV-Vis spectra of the photodegraded MNZ solutions **(A)** and the obtained C/Co values **(B).** All results were averaged based on triplicate measurements (Catalyst dose: 0.3 g/L, C_{MNZ}: 5 ppm, illumination time: 45 min) [70].

$E_{CB} = E_{VB} - E_g$. All data and information about these calculations are summarized in Table 1.

3.1.5. SEM-EDX and X-ray maps

Scanning electron microscopy (SEM) images for the binary AgBr/WO_3 sample are shown in Fig. 4 A-B. Spherical species were detected, relatively aggregated. As shown in Fig. 4C, particle size distribution show species are on the nanometer scale. EDX spectrum in Fig. 4D and Table SDT3 show the presence of all Ag, Br, O, and W atoms as constituent elements of the binary catalyst. To confirm the homogeneous distribution of the constituent elements in the binary catalyst, x-ray maps are presented in Fig. 4E and SDF3. All maps show a homogeneous distribution of the elements. Some SEM pictures, EDX data, and X-ray maps were also presented in the first part of the work [70].

3.2. Photocatalytic studies

3.2.1. Initial removal tests

The results obtained in the initial steps of the MNZ removal by different removal techniques of direct photolysis, surface adsorption, and heterogeneous photodegradation are presented in Fig. 5A. Comparing the spectra with that of a blank MNZ solution proves that the absorbance at a maximum peak wavelength of MNZ (λ_{max} = 320 nm) was decreased in all cases. This corresponds to the relative removal of MNZ molecules from the aqueous solution. Based on the negligible role of direct photolysis (around 1.7 % MNZ removal), the relative stability of MNZ molecules would be concluded against the arrived photons. On the other hand, no considerable bond breaking occurred in MNZ molecules via the direct photo-illumination process because if it occurred, it produced some radical species as initial sources for MNZ degradation [70].

The surface adsorption effect by individual and coupled catalysts was also studied. Comparing the results confirms that individual AgBr and WO_3 catalysts have no considerable photodegradation efficiencies because there is no significant change in the MNZ removal efficiencies achieved compared to the surface adsorption data. Comparing the individual catalysts, the binary AgBr:WO_3 catalyst showed better efficiency in MNZ removal than this catalyst's surface adsorption process. Based on the results, the suspensions were

Table 2
Some recent works in MNZ photodegradation.

Catalyst/Method	Procedure	Efficiency	Ref.
UiO-66-NH_2	Use of simulated solar light	>60 %	[106]
B–Sn/TiO_2	Different lights	96 % (10 ppm MNZ)	[107]
Heterogeneous Fenton-like Co-Cu catalysts	–	90 % of 12 ppm MNZ	[108]
MFe_2O_4@PC (M = Fe, Cu, Co, and Mn) composites	Visible light, heterogeneous photo-Fenton	96 % 300 ppm MNZ	[109]
TiO_2/Ag_3PO_4/g–C_3N_4	blue light-emitting diodes	97	[110]
Ce/SnO_2–Sb coated Ti-anode	Electro-Fenton process	37 TOC decrease	[111]
Fe^0/graphene-TiO_2 nanowires	20 W, W-Halogen, at 254 nm)	99 %	[112]
UV, Fenton/photo-Fenton	–	90 %	[113]

shaken at dark for 10 min to achieve the equilibrium adsorption/desorption state. After this step, the suspensions were subjected to the photodegradation process.

Due to this observed boosted photocatalytic activity of the binary catalyst in this initial step of the research (without no optimization), this catalyst was selected for further consideration. The boosted photocatalytic activity of the binary catalyst relates to the diminishing recombination of e/h charge carriers. This has been illustrated in the scavenging agents' section in the first part of the work [70].

It would be expected that the change in the amounts of each AgBr and WO_3 component in the coupled catalyst can change the photocatalytic activity of the prepared binary system. Thus, some binary catalysts with varied AgBr:WO_3 mole ratios were prepared as summarized in SDT 3. This case study is based on the fact that both the production extent of the photoinduced e/h pairs and their recombination extent can be affected by the amount of AgBr and WO_3 components in the binary catalysts. On the other hand, one component may be suitable for producing high amounts of e/h pairs due to the better-matched Eg with the arrived photon energies. Another component may be ideal as an electron acceptor or sink to consume the photoexcited electrons in the CB position of another element. This results in the rapid electron transfer between the C B position of component one and component two.

The change in the UV-Vis spectra of the photodegraded MNZ solutions by binary AgBr-WO_3 with various AgBr:WO_3 mole ratios in Fig. 5B confirms that the photocatalytic activity of the binary AgBr-WO_3 catalyst is an AgBr:WO_3 mole ratio-dependent property (Fig. 5B). Based on the above discussion, a balanced molar ratio between AgBr and WO_3 semiconductors in the binary catalyst should be provided to achieve the highest e/h pairs production with the lowest recombination extent. This was achieved when the moles of WO_3 in the binary catalyst were 3 times greater than that of the AgBr component. This is based on the catalyst's highest photocatalytic activity (or the lowest C/Co value) in MNZ photodegradation (Fig. 5C).

The effect of grinding time in the mechanical preparation of AgBr- WO_3 catalyst was also studied, and the results are presented in Fig. 6A. This change varies the photodegradation efficiency of the prepared binary catalyst. As shown in Fig. 6B, the best efficiency was obtained for 5 min grinding time. In this state, sufficient force induced the ingredients to diffuse relatively together for sufficient charge carrier transfer under illumination. High diffusion and contact would be expected at a longer grinding time, but the results are in the opposite trend. At longer times, the released heat may separate two ingredients and act as a single photocatalyst, decreasing the photodegradation efficiency.

3.2.2. Comparison with other works

Table 2 summarizes some recent published works in MNZ photodegradation by various photocatalysts. If good degradation efficiencies were obtained, some catalysts would be expensive or suffer from complex and expensive procedures. Titanium dioxide suffers from drawbacks like having a wide band gap in the UV region of light, consisting of about 4 % of solar light, difficulty separating its powder from the aqueous suspension, especially in nanoscale, etc. The Fenton process also has drawbacks like its efficiency dependence to the solution pH. Hence, acidic pH is needed to prevent iron hydroxide precipitation, producing a second sludge that requires a second removal treatment, etc. Instead, a simple procedure was used here to fabricate an effective binary catalyst.

4. Conclusions

The change in the crystallite sizes obtained by the Scherrer and W-H model can be related to the effect of the induced strain. In the DRS study, the band gap energies of 2.92 eV and 3.06 eV for WO_3, and AgBr-WO_3 confirm the goodness of the coupling to decrease the band gap energy. The boosted photocatalytic activity of the coupled catalysts in the photodegradation of metronidazole (MNZ) can be related to higher e/h separation in the coupled system. The e/h separation extent seems to depend on the maximum AgBr:WO_3 mole ratio in a 1:3 mol ratio. Grinding time applied to prepare the coupled catalyst also varied the photocatalytic activity. The best photocatalytic efficiency was obtained for 5 min grinding time. In this state, sufficient force induced the ingredients to diffuse relatively together for sufficient charge carrier transfer under illumination. High diffusion and contact would be expected at a longer grinding time, but the results are in the opposite trend. At longer times, the released heat may separate two ingredients and act as a single photocatalyst, decreasing the photodegradation efficiency.

CRediT authorship contribution statement

Elaheh Shabanian-Broujeni: Writing – original draft, Methodology, Data curation. **Alireza Nezamzadeh-Ejhieh:** Writing – review & editing, Supervision.

Declaration of competing interest

The authors declare that they have no known competing financial interests or personal relationships that could have appeared to influence the work reported in this paper.

Appendix A. Supplementary data

Supplementary data to this article can be found online at https://doi.org/10.1016/j.heliyon.2024.e31353.

References

[1] K. Liu, Z. Yin, R. Luo, B. Qiu, Y. Chen, C. Yang, Y. Luo, Z. Hong, M. Xue, Durable Co(OH)2/stearic acid-based superhydrophobic/superoleophilic nanocellulose membrane for highly efficient oil/water separation and simultaneous removal of soluble dye, Ind. Crop. Prod. 203 (2023) 117190.
[2] Z. Yin, Y. Cheng, Y. Deng, Z. Li, K. Liu, M. Li, X. Chen, M. Xue, J. Ou, S. Lei, Y. Luo, C. Xie, Z. Hong, Functional and versatile colorful superhydrophobic nanocellulose-based membrane with high durability, high-efficiency oil/water separation and oil spill cleanup, Surf. Coating. Technol. 445 (2022) 128714.
[3] Y. Deng, F. Xu, Z. Yin, M. Xue, Y. Chen, P. He, J. Wu, J. Ou, F. Wang, Y. Luo, Z. Hong, Controllable fabrication of superhydrophobic alloys surface on 304 stainless steel substrate for anti-icing performance, Ceram. Int. 49 (2023) 25135–25143.
[4] M. Malhotra, A. Sudhaik, Sonu, P. Raizada, T. Ahamad, V.-H. Nguyen, Q. Van Le, R. Selvasembian, A.K. Mishra, P. Singh, An overview on cellulose-supported photocatalytic materials for the efficient removal of toxic dyes, Ind. Crop. Prod. 202 (2023) 117000.
[5] K. Sharma, V. Hasija, M. Malhotra, P.K. Verma, A.A. Parwaz Khan, S. Thakur, Q. Van Le, H.H. Phan Quang, V.-H. Nguyen, P. Singh, P. Raizada, A review of CdS-based S-scheme for photocatalytic water splitting: synthetic strategy and identification techniques, Int. J. Hydrogen Energy 52 (2024) 804–818.
[6] W. Li, W. Li, X. Liu, H. Wu, J. Yang, F. Lu, L. Fan, A dual-responsive luminescent sensor for efficient detection of 3-nitrotyrosine and dipicolinic acid biomarkers based on copper(II) organic framework, Applied Organometallic Chemistry, n/a (2024) e7452.
[7] C. Hiller, U. Hübner, S. Fajnorova, T. Schwartz, J. Drewes, Antibiotic microbial resistance (AMR) removal efficiencies by conventional and advanced wastewater treatment processes: a review, Sci. Total Environ. 685 (2019) 596–608.
[8] Z. Li, Z. Yin, W. Xiao, Y. Chen, C. Yang, Y. Luo, Z. Hong, M. Xue, Facile construction of robust superhydrophobic ZIF-8@pulp/cellulose nanofiber (CNF) membrane for multifunctional applications, Ind. Crop. Prod. 209 (2024) 118001.
[9] M. Zheng, J. Chen, L. Zhang, Y. Cheng, C. Lu, Y. Liu, A. Singh, M. Trivedi, A. Kumar, J. Liu, Metal organic frameworks as efficient adsorbents for drugs from wastewater, Mater. Today Commun. 31 (2022) 103514.
[10] X. Dong, Y. Li, D. Li, D. Liao, T. Qin, O. Prakash, A. Kumar, J. Liu, A new 3D 8-connected Cd(ii) MOF as a potent photocatalyst for oxytetracycline antibiotic degradation, CrystEngComm 24 (2022) 6933–6943.
[11] L. Li, J. Zou, Y. Han, Z. Liao, P. Lu, A. Nezamzadeh-Ejhieh, J. Liu, Y. Peng, Recent advances in Al(iii)/In(iii)-based MOFs for the detection of pollutants, New J. Chem. 46 (2022) 19577–19592.
[12] C. El Bekkali, H. Bouyarmane, S. Laasri, A. Laghzizil, A. Saoiabi, Effects of metal oxide catalysts on the photodegradation of antibiotics effluent, Iran. J. Catal. 8 (2018) 241–247.
[13] H.A.-F. Khalaf, R.F.A. El-Baki, Effectiveness of ceria and stania nanoparticles in photodegradation tenoxicam antibiotics using UV-H2O2, Iran. J. Catal. 13 (2023) 285–297.
[14] T. Wang, Y. Wu, Y. Lin, X. Liu, X. Meng, Y. Wang, Enhanced tetracycline degradation performance of in-situ induced Ag/Cu2O composite by mussel, Water, Air, Soil Pollut. 235 (2024) 199.
[15] B. Gürcü, Y.B. Koca, M. Özkut, M.İ. Tuğlu, Matrix changes due to the toxic effects of metronidazole in intestinal tissue of fish (Onchorhynchus mykiss), Chemosphere 144 (2016) 1605–1610.
[16] I. Nasseh, M. Khodadadi, R. Khosravi, A. Beirami, N. Nasseh, Metronidazole removal methods from aquatic media: a systematic review, Ann. Med. Health Sci. Res. 14 (2016) e13756.
[17] A. Hayat, Alamgir, L. Huang, Z. Wang, R. Ullah, S. He, One-pot in situ synthesis of an NS-ligand co-doped metal–organic framework for the enhanced adsorption-assisted photocatalytic decontamination of metronidazole, RSC Adv. 14 (2024) 10229–10243.
[18] Z. Yin, X. Chen, T. Zhou, M. Xue, M. Li, K. Liu, D. Zhou, J. Ou, Y. Xie, Z. Ren, Y. Luo, Z. Hong, Mussel-inspired fabrication of superior superhydrophobic cellulose-based composite membrane for efficient oil emulsions separation, excellent anti-microbial property and simultaneous photocatalytic dye degradation, Separ. Purif. Technol. 286 (2022) 120504.
[19] Z. Yin, F. Yuan, M. Xue, Y. Xue, Y. Xie, J. Ou, Y. Luo, Z. Hong, C. Xie, A multifunctional and environmentally safe superhydrophobic membrane with superior oil/water separation, photocatalytic degradation and anti-biofouling performance, J. Colloid Interface Sci. 611 (2022) 93–104.
[20] M. Li, W. Liu, Z. Yin, H. Yang, Y. Chen, C. Yang, Y. Luo, Z. Hong, C. Xie, M. Xue, Facile fabrication of superhydrophobic and photocatalytic self-cleaning flexible strain sensor membrane for human motion, Sensor Actuator Phys. 363 (2023) 114750.
[21] A. Kumar, P. Singh, A.A.P. Khan, Q.V. Le, V.-H. Nguyen, S. Thakur, P. Raizada, CO2 photoreduction into solar fuels via vacancy engineered bismuth-based photocatalysts: selectivity and mechanistic insights, Chem. Eng. J. 439 (2022) 135563.
[22] D. Ye, L. Liu, Q. Peng, H. Qiu, H. Gong, A. Zhong, A. Liu, Effect of controlling thiophene rings on D-A polymer photocatalysts accessed via direct arylation for hydrogen production, Molecules 28 (11) (2023) 4507.
[23] M.J. Kadhim, M.A. Mahdi, A.M. Selman, S.J. Al-Ani, J.J. Hassan, N.M. Ahmed, The most important parameters that affect the photocatalytic activity of ZnO nanostructures against organic dyes: a review, Iran. J. Catal. 13 (2023) 1–21.
[24] F. Allawi Abdul Sajad, H.K. Egzar, M.A. Mahdi, Preparation and characterization of WO3 nanosheets and Au/WO3 nanocomposite for rabid photocatalytic degradation of methylene blue dye, Iran. J. Catal. 13 (2023) 319–330.
[25] E.T. Wahyuni, S. Wahyuni, M. Nora, N.D. Lestari, S. Suherman, Doping TiO2 by Cr from tannery wastewater for improving its activity under visible light in the dye degradation, Iran. J. Catal. 13 (2023) 169–176.
[26] N. Jasni, A. Iqbal, N. Abu Bakar, D.H. Yuli Yanto, H. Jia Yi, N.H. Mohd Kaus, M.N. Ahmad, S. Mulijani, Highly porous Bi (III) modified rice husk silica photocatalyst for the photocatalytic removal of cationic methylene blue, Iran. J. Catal. 13 (2023) 359–372.
[27] M.V. Kangralkar, M. Jayappa, Green synthesis of iron nanoparticles by Terminalia arjuna bark extract and photodegradation of rose bengal, Iran. J. Catal. 10 (2020) 181–188.

[28] S. Rajendran, M.M. Khan, F. Gracia, J. Qin, V.K. Gupta, S. Arumainathan, Ce3+-ion-induced visible-light photocatalytic degradation and electrochemical activity of ZnO/CeO2 nanocomposite, Sci. Rep. 6 (2016) 1–11.
[29] T.A. Saleh, V.K. Gupta, Photo-catalyzed degradation of hazardous dye methyl orange by use of a composite catalyst consisting of multi-walled carbon nanotubes and titanium dioxide, J. Colloid Interface Sci. 371 (2012) 101–106.
[30] K. Prakash, S. Karuthapandian, S. Senthilkumar, Zeolite nanorods decorated g-C3N4 nanosheets: a novel platform for the photodegradation of hazardous water contaminants, Mater. Chem. Phys. 221 (2019) 34–46.
[31] Y. Kumar, A. Sudhaik, K. Sharma, Sonu, P. Raizada, A. Aslam Parwaz Khan, V.-H. Nguyen, T. Ahamad, P. Singh, A.M. Asiri, Construction of magnetically separable novel arrow down dual S-scheme ZnIn2S4/BiOCl/FeVO4 heterojunction for improved photocatalytic activity, J. Photochem. Photobiol. Chem. 435 (2023) 114326.
[32] M. Yaghoubi-berijani, B. Bahramian, S. Zargari, The study of photocatalytic degradation mechanism under visible light irradiation on BiOBr/Ag nanocomposite, Iran. J. Catal. 10 (2020) 307–317.
[33] M.J. Kadhima, M.A. Mahdia, J.J. Hassana, Enhancing the photocatalytic performance of TiO2 nanoflower thin films under ultraviolet irradiation, Iran. J. Catal. 13 (2023) 437–448.
[34] N. Rouabah, R. Nazir, Y. Djaballah, A. Mir, I. Ameur, O. Beldjebli, Synthesis of a thin film of CuO/MgO/PVC nanocomposites for Photocatalytic applications, Iran, J. Catal. 13 (2023) 23–34.
[35] M. Li, W. Xiao, Z. Yin, Y. Chen, Y. Luo, Z. Hong, M. Xue, Construction of a robust MOF-based superhydrophobic composite coating with the excellent performance in antifouling, drag reduction, and organic photodegradation, Prog. Org. Coating 186 (2024) 108086.
[36] K. Sharma, A. Kumar, T. Ahamad, Q.V. Le, P. Raizada, A. Singh, L.H. Nguyen, S. Thakur, V.-H. Nguyen, P. Singh, Sulphur vacancy defects engineered metal sulfides for amended photo(electro)catalytic water splitting: a review, J. Mater. Sci. Technol. 152 (2023) 50–64.
[37] J. Wang, C. Rao, L. Lu, S. Zhang, M. Muddassir, J. Liu, Efficient photocatalytic degradation of methyl violet using two new 3D MOFs directed by different carboxylate spacers, CrystEngComm 23 (2021) 741–747.
[38] H.R. Pouretedal, M. Fallahgar, F. Sotoudeh Pourhasan, M. Nasiri, Taguchi optimization of photodegradation of yellow water of trinitrotoluene production catalyzed by nanoparticles TiO2/N under visible light, Iran. J. Catal. 7 (2017) 317–326.
[39] L.V. Thaninki, A. Samson Nesaraj, M. Arunkumar, Facile wet chemical synthesis and characterization of zinc doped gadolinium oxide nanoparticles for enhanced photodegradation of Rhodamine B dye under illumination of UV light, Iran. J. Catal. 12 (3) (2022) 315–336.
[40] F. Sanakousar, C. Vidyasagar, S.C. Swapna, V. Jiménez-Pérez, C. Viswanath, K. Prakash, M. Sridhara, Effect of surfactant on structural and optical properties of V2O5 nanocrystals as a potential catalyst for photodegradation, Iran. J. Catal. 1 (2023) 57.
[41] H.R. Pouretedal, M. Ahmadi, Preparation, Characterization and Determination of Photocatalytic Activity of MCM-41/ZnO and MCM-48/ZnO Nanocomposites, 2013.
[42] M.W. Kadi, A.A. Ismail, R.M. Mohamed, D.W. Bahnemann, Photodegradation of the herbicide imazapyr over mesoporous In2O3-TiO2 nanocomposites with enhanced photonic efficiency, Separ. Purif. Technol. 205 (2018) 66–73.
[43] A. Khalil, N.M. Aboamera, W.S. Nasser, W.H. Mahmoud, G.G. Mohamed, Photodegradation of organic dyes by PAN/SiO2-TiO2-NH2 nanofiber membrane under visible light, Separ. Purif. Technol. 224 (2019) 509–514.
[44] W. Shi, H. Lv, S. Yuan, H. Huang, Y. Liu, Z. Kang, Near-infrared light photocatalytic ability for degradation of tetracycline using carbon dots modified Ag/AgBr nanocomposites, Separ. Purif. Technol. 174 (2017) 75–83.
[45] K. Thirumalai, M. Shanthi, M. Swaminathan, Natural sunlight active GdVO4–ZnO nanomaterials for photo–electrocatalytic and self–cleaning applications, J. Water Proc. Eng. 17 (2017) 149–160.
[46] A. Malik, M. Nath, Multicore–shell nanocomposite formed by encapsulation of WO3 in zeolitic imidazolate framework (ZIF-8): as an efficient photocatalyst, J. Environ. Chem. Eng. 7 (2019) 103401.
[47] J. Behin, E. Ghadamnan, H. Kazemian, Recent advances in the science and technology of natural zeolites in Iran, Clay Miner. 54 (2019) 131–144.
[48] M. Shaban, M.R. Abukhadra, A. Hamd, Recycling of glass in synthesis of MCM-48 mesoporous silica as catalyst support for Ni2O3 photocatalyst for Congo red dye removal, Clean Technol. Environ. Policy 20 (2018) 13–28.
[49] M. Ghaedi, S. Hajjati, Z. Mahmudi, I. Tyagi, S. Agarwal, A. Maity, V. Gupta, Modeling of competitive ultrasonic assisted removal of the dyes–Methylene blue and Safranin-O using Fe3O4 nanoparticles, Chem. Eng. J. 268 (2015) 28–37.
[50] S.K. Tammina, B.K. Mandal, N.K. Kadiyala, Photocatalytic degradation of methylene blue dye by nonconventional synthesized SnO2 nanoparticles, Environ. Nanotechnol. Monit. Manag. 10 (2018) 339–350.
[51] G. Chen, M. Zhu, X. Wei, Photocatalytic properties of attached BiOCl-(0 0 1) nanosheets onto AgBr colloidal spheres toward MO and RhB degradation under an LED irradiation, Mater. Lett. 212 (2018) 182–185.
[52] V. Soni, A. Khosla, P. Singh, V.-H. Nguyen, Q.V. Le, R. Selvasembian, C.M. Hussain, S. Thakur, P. Raizada, Current perspective in metal oxide based photocatalysts for virus disinfection: a review, J. Environ. Manag. 308 (2022) 114617.
[53] C. Rao, L. Zhou, Y. Pan, C. Lu, X. Qin, H. Sakiyama, M. Muddassir, J. Liu, The extra-large calixarene-based MOFs-derived hierarchical composites for photocatalysis of dye: facile syntheses and contribution of carbon species, J. Alloys Compd. 897 (2022) 163178.
[54] A. Singh, A.K. Singh, J. Liu, A. Kumar, Syntheses, design strategies, and photocatalytic charge dynamics of metal–organic frameworks (MOFs): a catalyzed photo-degradation approach towards organic dyes, Catal. Sci. Technol. 11 (2021) 3946–3989.
[55] E.A. Nezamzadeh, Z. Banan, Kinetic Investigation of Photocatalytic Degradation of Dimethyldisulfide by Zeolite A Containing Nano CdS, 2012.
[56] A. Yousefi, A. Nezamzadeh-Ejhieh, Preparation and characterization of SnO2-BiVO4-CuO catalyst and kinetics of phenazopyridine photodegradation, Iran. J. Catal. 11 (2021) 247–259.
[57] T. Seyedi-Chokanlou, S. Aghabeygi, N. Molahasani, F. Abrinaei, Applying Taguchi method to optimize the synthesis conditions of ZrO2/TiO2/ZnO nanocomposite for high-performance photodegradation of Congo red, Iran. J. Catal. 11 (2021) 49–58.
[58] A. Selmi, H. Teymourinia, A. Zarei, M. Timoumi, A. Ramazani, CMCFO-Cr0. 1 Nanoferrites: sol-gel synthesis, structural, and magnetic studies: applications for photodegradation of Congo red dye, Iran. J. Catal. 12 (2022) 97–106.
[59] P. Zhou, F. Wang, Y. Shen, X. Duan, S. Zhao, X. Chen, J. Liang, Removal of emerging organic pollutants by zeolite mineral (clinoptilolite) composite photocatalysts in drinking water and watershed water, Catalysts 4 (2024) 216.
[60] L. Guo-Ping, L. Jie, L. Yun-Jun, AgBr nanoclusters: preparation by PAMAM dendrimers as template and photocatalytic property, Chin. J. Inorg. Chem. 23 (2007) 253–257.
[61] N. Kakuta, N. Goto, H. Ohkita, T. Mizushima, Silver bromide as a photocatalyst for hydrogen generation from CH3OH/H2O solution, J. Phys. Chem. B 103 (1999) 5917–5919.
[62] G. Li, K. Wong, X. Zhang, C. Hu, C.Y. Jimmy, R. Chan, P. Wong, Degradation of acid orange 7 using magnetic AgBr under visible light: the roles of oxidizing species, Chemosphere 76 (2009) 1185–1191.
[63] L. Zhang, K.-H. Wong, Z. Chen, C.Y. Jimmy, J. Zhao, C. Hu, C.-Y. Chan, P.-K. Wong, AgBr-Ag-Bi2WO6 nanojunction system: a novel and efficient photocatalyst with double visible-light active components, Appl. Catal. Gen. 363 (2009) 221–229.
[64] L.-S. Zhang, K.-H. Wong, H.-Y. Yip, C. Hu, J.C. Yu, C.-Y. Chan, P.-K. Wong, Effective photocatalytic disinfection of E. coli K-12 using AgBr− Ag− Bi2WO6 nanojunction system irradiated by visible light: the role of diffusing hydroxyl radicals, Environ. Sci. Technol. 44 (2010) 1392–1398.
[65] P. Wang, B. Huang, X. Zhang, X. Qin, Y. Dai, H. Jin, J. Wei, M.H. Whangbo, Composite semiconductor H2WO4· H2O/AgCl as an efficient and stable photocatalyst under visible light, Chem.–Eur. J. 14 (2008) 10543–10546.
[66] M. Gondal, M. Dastageer, A. Khalil, Synthesis of nano-WO3 and its catalytic activity for enhanced antimicrobial process for water purification using laser induced photo-catalysis, Catal. Commun. 11 (2009) 214–219.
[67] R. Victora, Calculated electronic structure of silver halide crystals, Phys. Rev. B 56 (1997) 4417.

[68] X. Zhang, L. Zhang, T. Xie, D. Wang, Low-temperature synthesis and high visible-light-induced photocatalytic activity of BiOI/TiO2 heterostructures, J. Phys. Chem. C 113 (2009) 7371–7378.
[69] J. Cao, B. Luo, H. Lin, S. Chen, Photocatalytic activity of novel AgBr/WO3 composite photocatalyst under visible light irradiation for methyl orange degradation, J. Hazard Mater. 190 (2011) 700–706.
[70] E. Shabanian-Boroujeni, A. Nezamzadeh-Ejhieh, The coupled WO3-AgBr nanocatalyst, part I: experimental design, kinetics and mechanism studies of the boosted photocatalytic activity towards metronidazole in an aqueous solution, J. Photochem. Photobiol. Chem. 446 (2024) 115148.
[71] D. Zhang, H. Tang, Y. Wang, K. Wu, H. Huang, G. Tang, J. Yang, Synthesis and characterization of graphene oxide modified AgBr nanocomposites with enhanced photocatalytic activity and stability under visible light, Appl. Surf. Sci. 319 (2014) 306–311.
[72] G.-H. He, G.-L. He, A.-J. Li, X. Li, X.-J. Wang, Y.-P. Fang, Y.-H. Xu, Synthesis and visible light photocatalytic behavior of WO3 (core)/Bi2WO6 (shell), J. Mol. Catal. Chem. 385 (2014) 106–111.
[73] A. Seyedeh, A. Mirsalari, Nezamzadeh-Ejhieh, the catalytic activity of the coupled CdS-AgBr nanoparticles: a brief study on characterization and its photodecolorization activity towards methylene blue, Desal, Water Treat. 175 (2020) 263–272.
[74] J. Sun, Y. Hou, Z. Yu, L. Tu, Y. Yan, S. Qin, S. Chen, D. Lan, H. Zhu, S. Wang, Visible-light-driven Z-scheme Zn3In2S6/AgBr photocatalyst for boosting simultaneous Cr (VI) reduction and metronidazole oxidation: kinetics, degradation pathways and mechanism, J. Hazard Mater. 419 (2021) 126543.
[75] J. Ding, Y. Chai, Q. Liu, X. Liu, J. Ren, W.-L. Dai, Selective deposition of silver nanoparticles onto WO3 nanorods with different facets: the correlation of facet-induced electron transport preference and photocatalytic activity, J. Phys. Chem. C 120 (2016) 4345–4353.
[76] F. Puga, J. Navío, M. Hidalgo, Features of coupled AgBr/WO3 materials as potential photocatalysts, J. Alloys Compd. 867 (2021) 159191.
[77] Z. Yin, M. Xue, Y. Luo, Z. Hong, C. Xie, Z. Ren, H. Wang, Excellent static and dynamic anti-icing properties of hierarchical structured ZnO superhydrophobic surface on Cu substrates, Chem. Phys. Lett. 755 (2020) 137806.
[78] M. Zebardast, A. Fallah Shojaei, K. Tabatabaeian, Enhanced removal of methylene blue dye by bimetallic nano-sized MOF-5s, Iran. J. Catal. 8 (2018) 297–309.
[79] M. Asgharian, M. Mehdipourghazi, B. Khoshandam, N. Keramati, Photocatalytic degradation of methylene blue with synthesized rGO/ZnO/Cu, Chem. Phys. Lett. 719 (2019) 1–7.
[80] P. Bindu, S. Thomas, Estimation of lattice strain in ZnO nanoparticles: X-ray peak profile analysis, Journal of Theoretical and Applied Physics 8 (2014) 123–134.
[81] Z. Yin, F. Yuan, D. Zhou, M. Xue, Y. Luo, Z. Hong, C. Xie, Ultra dynamic water repellency and anti-icing performance of superhydrophobic ZnO surface on the printed circuit board (PCB), Chem. Phys. Lett. 771 (2021) 138558.
[82] M. Que, W. Chen, P. Chen, J. Liu, X. Yin, B. Gao, W. Que, Effects of Zn2+ ion doping on hybrid perovskite crystallization and photovoltaic performance of solar cells, Chem. Phys. 517 (2019) 80–84.
[83] O. Kaygili, I. Ercan, T. Ates, S. Keser, C. Orek, B. Gunduz, T. Seckin, N. Bulut, L. Bañares, An experimental and theoretical investigation of the structure of synthesized ZnO powder, Chem. Phys. 513 (2018) 273–279.
[84] M. Chahkandi, M. Mirzaei, Structural and particle size evolution of sol–gel-derived nanocrystalline hydroxyapatite, J. Iran. Chem. Soc. 14 (2017) 567–575.
[85] D. Nath, F. Singh, R. Das, X-ray diffraction analysis by Williamson-Hall, Halder-Wagner and size-strain plot methods of CdSe nanoparticles-a comparative study, Mater. Chem. Phys. 239 (2020) 122021.
[86] N. Sawala, S. Omanwar, Study of energy transfer and spectral downshifting in Ce, RE (RE= Nd and Yb) co-doped lanthanum phosphate, Chem. Phys. 485 (2017) 9–12.
[87] M. Sundararajan, V. Sailaja, L.J. Kennedy, J.J. Vijaya, Photocatalytic degradation of rhodamine B under visible light using nanostructured zinc doped cobalt ferrite: kinetics and mechanism, Ceram. Int. 43 (2017) 540–548.
[88] S. Ilyas, B. Abdullah, D. Tahir, X-ray diffraction analysis of nanocomposite Fe3O4/activated carbon by Williamson–Hall and size-strain plot methods, Nano-Structures & Nano-Objects 20 (2019) 100396.
[89] V.B. Kumar, D. Mohanta, Formation of nanoscale tungsten oxide structures and colouration characteristics, Bull. Mater. Sci. 34 (2011) 435–442.
[90] J. Qin, N. Chen, C. Feng, C. Fan, Y. Gao, Synthesis of a high-performance silver silicate (Ag6Si2O7)/silver bromide (AgBr) photocatalyst with enhanced visible light catalytic activity for refractory organic pollutants, Colloids Surf. A Physicochem. Eng. Asp. 577 (2019) 213–223.
[91] X. Chen, Z. Yin, J. Yan, M. Xue, Y. Chen, C. Yang, Y. Luo, Fabrication of ZnO@Fe2O3 superhydrophobic coatings with high thermal conductivity, Surf. Coating. Technol. 467 (2023) 129701.
[92] X. Chen, Z. Yin, Y. Deng, Z. Li, M. Xue, Y. Chen, Y. Xie, W. Liu, P. He, Y. Luo, Z. Hong, C. Xie, Harsh environment-tolerant and robust superhydrophobic graphene-based composite membrane for wearable strain sensor, Sensor Actuator Phys. 362 (2023) 114630.
[93] S. Noreen, H.N. Bhatti, M. Iqbal, F. Hussain, F.M. Sarim, Chitosan, starch, polyaniline and polypyrrole biocomposite with sugarcane bagasse for the efficient removal of Acid Black dye, Int. J. Biol. Macromol. 147 (2020) 439–452.
[94] S. Bock, C. Kijatkin, D. Berben, M. Imlau, Absorption and remission characterization of pure, dielectric (nano-) powders using diffuse reflectance spectroscopy: an end-to-end instruction, Appl. Sci. 9 (2019) 4933.
[95] M. Sabonian, K. Mahanpoor, Preparation of ZnO nanocatalyst supported on todorokite and photocatalytic efficiency in the reduction of chromium (VI) pollutant from aqueous solution, Iran. J. Catal. 9 (2019) 201–211.
[96] J. Chen, G. Wang, J. Wei, Y. Guo, Effect of sulfur dopant atoms on the electronic band gap and optical properties of tin iodide, Chem. Phys. Lett. 730 (2019) 557–561.
[97] S. Dianat, Visible light induced photocatalytic degradation of direct red 23 and direct brown 166 by InVO4-TiO2 nanocomposite, Iran. J. Catal. 8 (2018) 121–132.
[98] S.K. Suram, P.F. Newhouse, J.M. Gregoire, High throughput light absorber discovery, Part 1: an algorithm for automated Tauc analysis, ACS Comb. Sci. 18 (2016) 673–681.
[99] P. Norouzzadeh, K. Mabhouti, M. Golzan, R. Naderali, Investigation of structural, morphological and optical characteristics of Mn substituted Al-doped ZnO NPs: a Urbach energy and Kramers-Kronig study, Optik 204 (2020) 164227.
[100] P. Makuła, M. Pacia, W. Macyk, How to correctly determine the band gap energy of modified semiconductor photocatalysts based on UV–vis spectra, J. Phys. Chem. Lett. 9 (2018) 6814–6817.
[101] J. Tauc, in: F. Abeles (Ed.), Chap. 5 of" Optical Properties of Solids", North-Holland Publishing Company, Amsterdam, 1972.
[102] J.B. Coulter, D.P. Birnie III, Assessing Tauc plot slope quantification: ZnO thin films as a model system, Phys. Status Solidi 255 (2018) 1700393.
[103] R. Köferstein, L. Jäger, S.G. Ebbinghaus, Magnetic and optical investigations on LaFeO3 powders with different particle sizes and corresponding ceramics, Solid State Ionics 249–250 (2013) 1–5.
[104] R. Köferstein, S.G. Ebbinghaus, Investigations of BaFe0.5Nb0.5O3 nano powders prepared by a low temperature aqueous synthesis and resulting ceramics, J. Eur. Ceram. Soc. 37 (2017) 1509–1516.
[105] K.-i. Katsumata, R. Motoyoshi, N. Matsushita, K. Okada, Preparation of graphitic carbon nitride (g-C3N4)/WO3 composites and enhanced visible-light-driven photodegradation of acetaldehyde gas, J. Hazard Mater. 260 (2013) 475–482.
[106] Y.L. Wang, A. Gómez-Avilés, S. Zhang, J.J. Rodriguez, J. Bedia, C. Belver, Metronidazole photodegradation under solar light with UiO-66-NH2 photocatalyst: mechanisms, pathway, and toxicity assessment, J. Environ. Chem. Eng. 11 (2023) 109744.
[107] S.A. Fahim, N. Zahan, R.A. Shathy, M.S. Quddus, M. Moniruzzaman, S.M. Masum, M.A.I. Molla, B–Sn/TiO2 nanoparticles for photodegradation of metronidazole antibiotics under different lights, Mater. Chem. Phys. 305 (2023) 127937.

[108] L. Liu, J. Li, X. Guo, H. Wu, J. Wu, Y. Dong, Y. Li, Y. Lu, Enhanced performance of heterogeneous fenton-like Co-Cu catalysts for metronidazole degradation: ethylene glycol as a superior fabrication solvent, J. Environ. Chem. Eng. 11 (2023) 110597.
[109] H. Cai, T. Zhao, Z. Ma, Synthesis of magnetic MFe2O4@PC (M = Fe, Cu, Co, and Mn) composites and application of heterogeneous photo-Fenton efficient removal of metronidazole under visible light, J. Ind. Eng. Chem. 121 (2023) 322–330.
[110] H. Abbasi-Asl, M.M. Sabzehmeidani, M. Ghaedi, Efficient degradation of metronidazole antibiotic by TiO2/Ag3PO4/g–C3N4 ternary composite photocatalyst in a continuous flow-loop photoreactor, J. Environ. Chem. Eng. 9 (2021) 105963.
[111] W. Cheng, M. Yang, Y. Xie, B. Liang, Z. Fang, E.P. Tsang, Enhancement of mineralization of metronidazole by the electro-Fenton process with a Ce/SnO2–Sb coated titanium anode, Chem. Eng. J. 220 (2013) 214–220.
[112] X. Wang, A. Wang, M. Lu, J. Ma, Synthesis of magnetically recoverable Fe0/graphene-TiO2 nanowires composite for both reduction and photocatalytic oxidation of metronidazole, Chem. Eng. J. 337 (2018) 372–384.
[113] H. Shemer, Y.K. Kunukcu, K.G. Linden, Degradation of the pharmaceutical Metronidazole via UV, Fenton and photo-Fenton processes, Chemosphere 63 (2006) 269–276.